PHYSICAL REVIEW MATERIALS **9**, 064601 (2025)

EXAFS sheds light on short-range ordering in $\mathrm{Ge}_{1-x}\mathrm{Sn}_x$ heteroepitaxial layers grown by MBE and CVD

Sliman Gougam,[1,*,†] Francesco De Angelis,[2,*] Carlo Meneghini,[2] Omar Concepción,[3] Dan Buca,[3]
Giovanni Capellini,[1,2] and Marvin H. Zoellner[1,‡]
[1] *IHP - Leibniz Institute for High Performance Microelectronics, Im Technologiepark 25, 15236 Frankfurt (Oder), Germany*
[2] *Dipartimento di Scienze, Università Roma Tre, Viale G. Marconi 446 Roma 00146, Italy*
[3] *Peter Grünberg Institute 9 (PGI-9) and JARA-Fundamentals of Future Information Technologies, 52428 Jülich, Germany*

(Received 13 December 2024; accepted 19 May 2025; published 2 June 2025)

The local arrangement of atoms in an alloy impacts its electronic band structure and, consequently, its fundamental physical properties. This work investigates the short-range order of tin atoms in binary $\mathrm{Ge}_{1-x}\mathrm{Sn}_x$ semiconductors epitaxially grown on Ge-buffered Si (001) substrates. Samples featuring Sn content up to 13 at.% were analyzed by x-ray absorption fine structure spectroscopy at the Sn-K edge. The study reveals how the growth method and its process parameters, like temperature, or the epitaxial built-up strain affect the local atomic ordering of tin within the alloys. While the deposition technique seems to have a marginal effect on the Sn short-range ordering, the growth temperature and Sn content systematically influence the bonding angles Sn. Ge-Sn next neighbor coordination shells, whereas the interatomic distances remain largely unaffected. In the first coordination shell Sn-Ge are strongly favored over Sn-Sn, while the opposite happens in the next coordination shell, where Sn-Sn are systematically favored. These insights into the relationship of growth condition and layer properties enable to identify the nature of the large variety of electronic and optical properties measured in $\mathrm{Ge}_{1-x}\mathrm{Sn}_x$ layers.

DOI: 10.1103/PhysRevMaterials.9.064601

I. INTRODUCTION

Within the last decade, there has been a remarkable rise in interest surrounding new semiconductors of group IV elements. In this respect, $\mathrm{Ge}_{1-x}\mathrm{Sn}_x$ semiconductor alloys are seen as the alloys that may potentially lead to monolithic integration of a broad range of applications in electronics, optoelectronics, spintronics, and thermoelectric using the mature Si technological platform [1–7]. The driving force is their peculiar electronic band structure which can be largely tuned by varying the Sn content and the strain condition [8]. Notably, a direct fundamental bandgap is achieved in strain-relaxed $\mathrm{Ge}_{1-x}\mathrm{Sn}_x$ alloys for Sn content above 8 at.% or even lower values under biaxial tensile strain conditions [9]. This peculiar physical property has been very successfully exploited to demonstrate group IV-based optical lasers operating at RT [9] and electrically pumped disk lasers based on the same material system [2,10].

The growth of $\mathrm{Ge}_{1-x}\mathrm{Sn}_x$ is a major challenge due to the low solid solubility of Sn in Ge (Sn < 1 at.%) and to the large lattice mismatch between α-Sn and both Si and Ge of approximately 20% and 15%, respectively [11,12]. Therefore, growth conditions at far nonthermodynamic equilibrium are required for the epitaxy of $\mathrm{Ge}_{1-x}\mathrm{Sn}_x$ alloys with Sn concentrations beyond the solubility limit [11].

Molecular beam epitaxy (MBE) and chemical vapor deposition (CVD) are the most common growth methods for the epitaxy of $\mathrm{Ge}_{1-x}\mathrm{Sn}_x$ layers, but the growth mechanism and their precursors type differ significantly. CVD uses gas precursors and features a relatively fast growth rate (>10 nm/min) and enables growth at relatively high temperatures ($T > 300\,^{\circ}\mathrm{C}$). To date is the only growth method offering high crystallinity material suitable for photonic applications [13,14]. MBE offers the potential for very low-temperature growth ($<200\,^{\circ}\mathrm{C}$), enabling the growth of $\mathrm{Ge}_{1-x}\mathrm{Sn}_x$ layers with Sn content up to 25 at.% [15]. However, achieving thick and strain-relaxed $\mathrm{Ge}_{1-x}\mathrm{Sn}_x$ film remains unattainable by MBE due to epitaxial breakdown induced by kinetic surface roughening [16,17].

The distribution of Sn atoms within the Ge crystal lattice plays an important role in defining the physical properties of $\mathrm{Ge}_{1-x}\mathrm{Sn}_x$ films [18]. For instance, Sn clustering or short-range ordering (SRO) in $\mathrm{Ge}_{1-x}\mathrm{Sn}_x$ thin films has been shown to affect the electrical and optical properties, the bowing parameters [19], and the electronic band structure as a whole [20]. Several groups have recently started addressing this issue using different experimental methods sensitive to the local arrangement of atoms. Corley-Wiciak *et al.* used polarization-resolved Raman spectroscopy to evidence a nonrandom atomic distribution in the lattice through Sn atoms SRO with Sn-Sn repulsion [18]. Liu *et al.* [21] found via atom probe tomography (APT) a weak Sn-Sn atoms correlation, which depends on depth and strain in the layer along the

---

[*] These authors contributed equally to this work.

[†] Contact author: gougam@ihp-microelectronics.com

[‡] Contact author: zoellner@ihp-microelectronics.com

growth direction, but not on the average film composition. Further, APT studies were carried out to compare the SRO of $Ge_{1-x}Sn_x$ grown by MBE and CVD [22] with Sn composition ranging from 7 to 20 at.%, showing a stronger preference for Sn-Sn first nearest neighbor (1NN) formation in MBE $Ge_{1-x}Sn_x$ as compared to the CVD counterpart [22]. Mukherjee *et al.* [23] also found via APT a homogeneous distribution in CVD grown $Ge_{1-x}Sn_x$ films but SRO indication in ternary SiGeSn alloys. HAADF-STEM is a method that investigates local Sn distribution in GeSn alloys, utilizing atomic number contrast to visualize nanoscale inhomogeneities. Combined with energy-dispersive x-ray spectroscopy (EDS), it has been used to assess Sn incorporation, defect formation, and strain relaxation mechanisms. This approach gives direct insights into Sn clustering, compositional gradients, and their correlation with the structural and optoelectronic properties of GeSn films [24,25].

From the modeling point of view, density functional theory (DFT) studies indicate a much higher degree of SRO, characterized by suppression of Sn-Sn nearest neighbor correlations, with the redistribution of these Sn atoms to the third shell [26]. In a more recent paper, two types of SRO possibly coexisting in $Ge_{0.75}Sn_{0.25}$ layers, namely regular short-range order (R-SRO) and enhanced short-range order (E-SRO) [20], have been reported together with their impact on the electronic band structure [20].

X-ray absorption fine structure (XAFS) spectroscopy is an alternative method, particularly suitable for studying local ordering phenomena in alloys, as its chemical selectivity and local structure sensitivity allow information to be obtained about the chemical species, number, and distance between neighboring atoms around the absorbing atomic species [27,28]. In contrast to diffraction, where the signal originates from structures exhibiting translational symmetry, the XAFS signal is derived from the relative position of the atoms around the absorber, thereby offering complementary insights with respect to diffraction [29]. Extended x-ray absorption fine structure (EXAFS) has been used previously to study changes in bond lengths as a function of composition in pseudomorphic $Ge_{1-x}Sn_x$ films [30,31]. In an EXAFS study, Gencarelli *et al.* showed the presence of a short-range order in a $Ge_{1-x}Sn_x$ epitaxial layer deposited by CVD on Ge/Si virtual substrates, with a reduction of the coordination number of the Sn following a repulsion of Sn pairs [27]. The reports on EXAFS studies on MBE-grown $Ge_{1-x}Sn_x$ layers [30,31], however, have no conclusive assessment of the impact of growth parameters or the Sn content on the local crystalline structure. Please note that no direct comparison between MBE and CVD grown $Ge_{1-x}Sn_x$ sample within a single EXAFS measurement campaign is available, insofar. To address this gap, in this study, Sn K-edge EXAFS is employed to compare the short-range order behavior of a series of MBE and CVD grown $Ge_{1-x}Sn_x$ heteroepitaxial layers. In particular, the impact of Sn content, growth temperature, composition, and strain relaxation on the short-range order is here investigated.

II. EXPERIMENTAL DETAILS

$Ge_{1-x}Sn_x$ heteroepitaxial thin films were grown on 1.5 μm Ge buffers on Si(001) substrates using MBE system under ultrahigh vacuum (UHV) conditions with a base pressure of $< 2 \cdot 10^{-9}$ mbar. A dual filament effusion cell and electron beam evaporator were employed for Sn and Ge evaporation, respectively. In addition, two samples were grown with chemical vapor deposition (CVD) [6] for comparison with MBE grown $Ge_{1-x}Sn_x$ samples (Table I). For CVD growth an industry-compatible 300 mm/200 mm AIXTRON TRICENT reduced-pressure CVD (RP-CVD) reactor was used. The $Ge_{1-x}Sn_x$ epitaxy exhibits varying Sn contents from 7.4 at.% to 13.4 at.% and thicknesses ranging from 50 nm to 290 nm. $Ge_{1-x}Sn_x$ layers composition was measured using Rutherford backscattering spectroscopy (RBS) and confirmed by x-ray diffraction (XRD). The quadratic formula $a_{\mathrm{GeSn}} = 5.658 + 0.872x - 0.041x^2$ is used for the calculation of Sn content while experimental bowing parameter of 0.041 is used to calculate the Sn content [32]. Furthermore, a tetragonal distortion related to biaxial strain was assumed. X-ray absorption spectroscopy (XAS) measurements were performed at the BM08-LISA [33] beamline (Experiment Nr. MA5463) of the European Synchrotron Radiation Facility (ESRF) in Grenoble, France. Beamline optics include a Si (111) double crystal, fixed exit monochromator and pair of Pt coated mirrors, a first collimating mirror before the monochromator, and a second mirror, toroidal bent after the monochromator focuses the beam on the sample.

Sn-K edge (29.200 keV) XAS signals were measured in fluorescence mode using an ultrapure nine-channel Ge multidetector. Spectra extend up to about 800 eV above the edge corresponding to the photoelectron wave vector around $k = 15$ Å^{-1}. XAS measurements were performed keeping the sample at liquid nitrogen temperature, and the sample surface oriented at a grazing incidence angle of approximately $10 - 15^{\circ}$ with respect to the incident x-ray beam direction, to maximize the fluorescence signal from the thin $Ge_{1-x}Sn_x$ films.

The fluorescence signals present spikes coming from the Bragg peak from the thin film substrates. Three to eight scans were measured slightly tilting the sample around the vertical axis ($\pm 3^{\circ}$) allowing to individuate the Bragg peaks comparing the signals from different detectors/scans, and then to remove them cutting only specific regions of each signal, so optimizing the data collection and statistics [34]. The x-ray beam energy calibration was ensured by monitoring the x-ray absorption near edge structure (XANES) spectra from a Sn reference foil regularly during the experiment. Data reduction of the experimental x-ray absorption spectra was performed with the program ESTRA [35]. The ESTRA program allows the data average and extraction of the EXAFS structural signal $\chi(k)$ following standard procedures which include linear pre-edge subtraction, edge jump discontinuity normalization, and bare atom background subtraction. The edge energy, E_o, used to define the photoelectron wave vector $k = \sqrt{[2m_e(E_{hv} - E_0)]/\hbar^2}$ with m_e being the electron mass and E_{hv} the x-ray beam energy was selected at half of the absorption edge discontinuity and refined during the analysis. The data in the near edge XANES region provides useful information to compare the valence state and coordination geometry of Sn atoms in different samples. The experimental EXAFS signals were quantitatively analyzed using the FitEXA program [35], which enabled the fitting of the raw

TABLE I. Summary of $Ge_{1-x}Sn_x$ materials growth condition and analysis of the Sn K-edge EXAFS. The $Ge_{1-x}Sn_x$ samples name convention is arranged in two classes, "M" samples represent the MBE grown $Ge_{1-x}Sn_x$ layers, while "C" samples correspond to CVD grown $Ge_{1-x}Sn_x$ layers. Sample name also includes Sn composition and growth temperature, for example, M7-200 is an MBE sample with a Sn content of 7.4% and a temperature of 200 °C.

Sample	M7-200	M9-200	M11-200	M13-200	M7-100	C11-330	C12-360
Roughness (nm)	0.4	0.4	0.5	0.6	0.6		
XRD at. % Sn	7.4	8.9	11.2	13.4	7.4	11.1	12.0
Sn K-cell Temp. (°C)	990	1001	1010	1022.5	990		
h (nm)	93	87	80	50	98	90	290
Growth. Temp. (°C)	200	200	200	200	100	330	360
Strain (%)	−0.98	−1.2	−1.52	−1.59	−0.97	−1.51	−0.62
Rel. GeSn/Ge (%)	0	0	0	15	0	0	61

experimental data to the model curves in k space using nonlinear least-squares algorithms implemented in the MINUIT library [36]. The model EXAFS curves are calculated using the standard EXAFS formula [37] with Gaussian disorder approximation. The photoelectron amplitude and phase functions were calculated for representative atomic clusters using the FEFF8.2 program [38]. The signals used for refinements were selected through an iterative process, ensuring their statistical significance and physical consistency. Only single scattering contributions were considered, as multiple scattering contributions were determined to be negligible owing to the absence of (near-)collinear atomic arrangements (focusing effects) in the structure. Constraints were imposed upon the refined parameters (see below) to reduce parameter correlations.

Energy dispersive x-ray (EDX) analysis, atomic force microscopy (AFM), and x-ray diffraction (XRD) reciprocal space maps were performed to complete the material characterization regarding elemental distribution, sample roughness, and lattice strain.

III. RESULTS AND DISCUSSION

The physical characterization of the $Ge_{1-x}Sn_x$ samples discussed in this study is summarized in Table I.

Accurate analysis of the EXAFS spectra was performed using a multishell refinement. The structural parameters obtained, specifically interatomic distances (R), coordination numbers (N), and mean square relative displacement factors (σ^2), characterizing the local environment around the average Sn absorber, are presented in Table II. The physical characterization of the $Ge_{1-x}Sn_x$ samples discussed in this study and the growth conditions are summarized in Table I. The basis of the fitting model relies on the Ge crystal structure of the FCC diamond cubic, with a total of four atoms in the first shell and 12 atoms in the second shell.

A. Sample structure and morphology

To facilitate a direct comparison as a function of Sn content M7-200, M9-200, and M11-200 were grown at the same growth temperature (200 °C) and Ge deposition rate (0.25 Å/s) targeting different compositions in the 7–11 at.% range and the same nominal thickness of 90 nm. Sample M13-200 $Ge_{0.87}Sn_{0.13}$ is pseudomorphic grown on Ge to a thickness of only 50 nm to avoid plastic strain relaxation but is thick enough to be investigated in EXAFS. The exemplary layer quality of sample M11-200 is shown in Fig. 1. The structural properties and Sn concentration is extracted from XRD-RSM in the symmetric (004) and the asymmetric (224) diffractions. The asymmetric (224) diffraction is shown in Fig. 1(a). The diffraction peaks are in plane aligned with the Ge buffer indicating pseudomorphic growth. The homogeneous Sn distribution within the epilayers is demonstrated by the EDX elemental analyses [Fig. 1(b)]. Moreover, Fig. 1(c) shows surface topology measured by AFM in a 2 μm scale. The spotty RHEED pattern appears as shown in inset Fig. 1(c) is an indication of epitaxial crystalline growth with a rough surface.

B. The local structure around Sn, XAFS Analysis

The Sn K-edge normalized XANES spectra measured on all the $Ge_{1-x}Sn_x$ films are presented in Fig. 2 along with their first derivative. The XANES spectra show no changes in shape or position. The good reproducibility and energy alignment show the same oxidation states of Sn and its electronic behavior in all MBE and CVD samples despite their deposition parameter changes.

The Ge crystal phase has a diamond cubic structure, Fd-3m, with lattice parameter $a_{Ge} = 5.66$ Å with each Ge atom covalently bonded to four other Ge at $R_{GeGe} = 2.46$ Å in a tetrahedral arrangement as suggested in literature [39]. Four atoms are assumed in the first shell and the second shell is made by 12 atoms. The 12 next neighbors connected through the Ge-Ge-Ge path with a tetrahedral bond angle $\theta_{Ge} = 109.45°$. Sn has two potential crystallographic structures: (i) α-Sn, which is similar To Ge, with Fd-3m cubic symmetry and tetrahedral coordination, with a larger lattice parameter $a_{Sn} = 6.47$ Å and $R_{SnSn} = 2.84$ Å; and (ii) β-Sn with a tetragonal structure, I41/amd, with Sn bonded to four neighbors forming flattened tetrahedra at larger distances $R_{SnSn}^{Tetragonal} = 3.05$ Å [40]. It is noteworthy that the interatomic distances determined through EXAFS may slightly deviate from those obtained from XRD. This difference, which can be significantly larger than the statistical uncertainty, stems from an intrinsic difference between the two techniques [41]. The diffraction signal is inherently dependent on the long-range order of the sample, revealing only structural features that exhibit translational symmetry. Consequently, diffraction

TABLE II. Results of the Sn K-edge EXAFS data analysis on the investigated samples. The thin films growth parameter is resumed on the top, for the convenience of the readers. For each shell (1–3) the structural parameters are reported, namely coordination (multiplicity) numbers N, distances R, and mean square relative displacement σ^2 for the Ge or Sn neighbors. Uncertainties on the last digit of the refined parameters are shown in parenthesis, and constrained fixed parameters (see text) are labeled by *.

	Sample		*(M7-200)*	*(M9-200)*	*(M11-200)*	*(M13-200)*	*(M7-100)*	*(C11-330)*	*(C12-360)*
		Deposition	MBE	MBE	MBE	MBE	MBE	CVD	CVD
		Sn (at. %)	7.4	8.9	11.2	13.4	7.4	11.1	12
		d (nm)	93	87	80	50	98	90	290
		Strain (%)	−0.98	−1.2	−1.52	−1.59	−0.97	−1.51	−0.62
		T (°C)	200	200	200	200	100	330	360
Shell 1	Sn_1	N	0.4(1)				0.3(1)		
		R (Å)	2.85(2)				2.83(2)		
		σ^2(x10^3 Å^2)	4.0(3)				4.0(3)		
	Ge_1	N	3.6*	4*	4*	4*	3.7*	4*	4*
		R (Å)	2.57(1)	2.59(1)	2.59(1)	2.59(1)	2.57(1)	2.58(1)	2.59(1)
		σ^2(x10^3 Å^2)	1.7(2)	2.3(2)	1.9(2)	3.1(3)	1.4(2)	2.1(2)	2.9(3)
Shell 2	Sn_2	N	5.4(3)	4.6(3)	4.6(3)	3.8(3)	4.9(3)	4.6(3)	3.3(2)
		R (Å)	3.99(2)	4.09(3)	4.11(3)	4.09(2)	3.98(2)	4.11(3)	4.15(2)
		σ^2(x10^3 Å^2)	2.0(2)	3.2(2)	5.9(3)	12(1)	6.2(2)	5.9(3)	10(1)
	Ge_2	N	6.6*	7.4*	7.4*	8.2*	7.2*	7.4*	8.8*
		R (Å)	4.02(2)	4.09(2)	4.10(2)	4.06(2)	4.06(2)	4.09(2)	4.10(2)
		σ^2(x10^3 Å^2)	2.0*	3.2*	5.9*	12*	6.2*	5.9*	10*
Shell 3	Ge_3	N	12*	12*	12*	12*	12*	12*	12*
		R (Å)	4.81(2)	4.88(2)	4.87(2)	4.83(3)	4.80(3)	4.86(2)	4.81(3)
		σ^2(x10^3 Å^2)	17(1)	12(2)	16(2)	21(2)	16(2)	19(2)	22(2)

data should be interpreted more precisely as distances between lattice positions, corresponding to the average atomic positions within the unit cell. In contrast, the XAFS signal provides direct information about the local atomic environment, specifically the interatomic distances between the absorbing atom and its neighboring atoms, independently of the long-range order in the sample [29]. The quantitative data analysis has been carried out fitting the k-weighted experimental spectra in the 3 Å^{-1} to 13 Å^{-1} range, balancing the demand for a wider k range, high resolution, with the need for low noise data (restricted k range) for better reliability of the results. To fit the EXAFS spectra, Sn is assumed to be substitutionally incorporated in the Ge cubic lattice and, starting from the first coordination shell, signals were progressively added verifying their statistical significance (F test). The k^2-weighted experimental EXAFS spectra $k^2\chi_{\text{exp}}$ and the moduli of their Fourier transforms (|FT|) are shown in Fig. 3 along with their best-fit curves. The Fourier transforms provide a more intuitive description of the Sn local atomic structure in the films, though the phase shift effect shortens the |FT| peak position by roughly 0.5 Å: the main peak in the |FT| represents the position of the nearest neighbor shell. The next neighbor shells are evident but clearly weaker as a result of a number of concomitant factors, including the reduced photoelectron mean free path, natural attenuation of spherical photoelectron waves ($\sim R^{-2}$), and structural disorder [37]. The best-fit results are resumed in Table II.

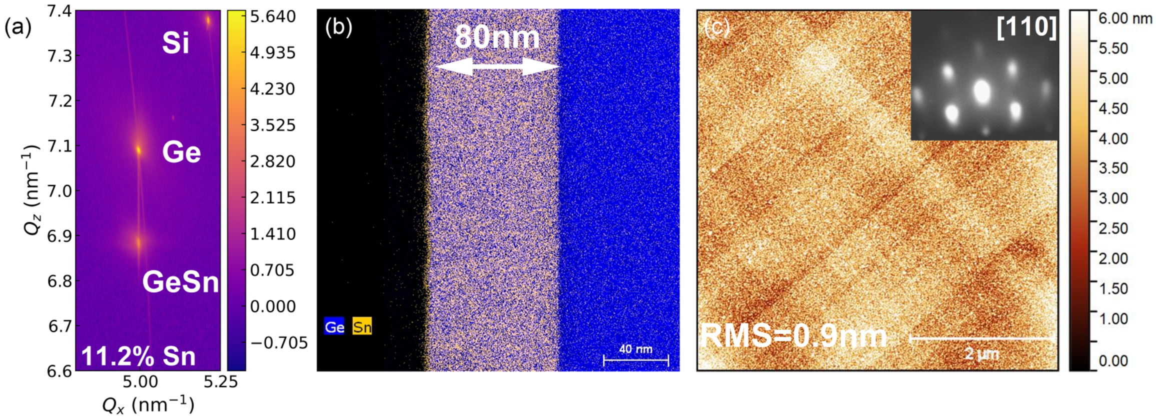

FIG. 1. (a) XRD 2D-RSM around (224) Bragg reflections of the sample with 11.2% of Sn concentration. The signals originating from the Si substrate, the Ge buffer, and the $Ge_{1-x}Sn_x$ epilayer are labeled accordingly in the figure. (b) EDX image of sample M11-200. (c) AFM image of sample M11-200 with 5 µm field of view and a RHEED image along [110] as inset.

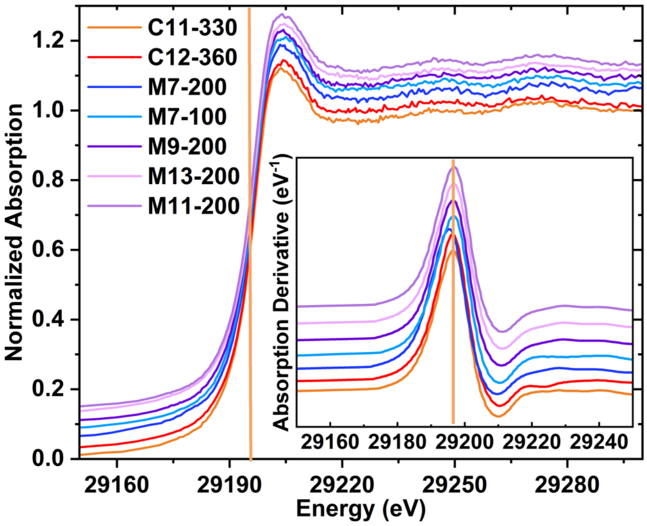

FIG. 2. XANES spectra of all the investigated samples. XANES derivatives are presented in the inset. No changes are evident in the position of the raising edge, pointing out no changes in the Sn valence state. Only minor changes are visible in the near post-edge region, indicating minor changes in the Sn local coordination geometry between the different samples.

The three main shells are found to be statistically significant to fit the experimental data, which allows to describe the average local atomic structure around Sn till about 5 Å. After preliminary tests, the same energy shift of $\Delta E = 8$ eV and $S_o^2 = 1.1$ was used for all the analysis, which guarantees high sensitivity to slight changes in the structural parameters between the samples. Constraints based on the crystallographic models are applied to reduce the correlation among the parameters. Specifically, the total multiplicities (N) of each coordination shell were fixed to their crystallographic values: $N_1 = 4$, $N_2 = 12$, $N_3 = 12$, the number of Sn and Ge atoms given by $N_{\mathrm{Sn}} = x_i \cdot N_i$ and $N_{\mathrm{Ge}} = (1 - x_i) \cdot N_i$ (i = 1, 2), were obtained by refining the free parameters x_i, representing the fraction of Sn-Sn neigbours in the ith shell. For all the samples, excluding M7-200 and M7-100, attempts to include $\mathrm{Sn-Sn_1}$ contributions in the first shell ($x_1 > 0$) worsen the fit. Therefore, the parameter x_1 was fixed zero for these samples. In the thicker MBE samples M7-200 and M7-100, a statistically significant proportion of $\mathrm{Sn-Sn_1}$ neighbors, approximately $x_1 \simeq 10\%$, was observed (Table II). Therefore, the nearest neighbor coordination numbers were fixed to four in all these samples.

For the second shell, the $\mathrm{Sn-Ge_2}$ and $\mathrm{Sn-Sn_2}$ EXAFS signals are strongly in antiphase, especially in the high energy (high-k) region of the spectra, resulting in a strong correlation between the disorder parameters for $\mathrm{Sn_2}$ and $\mathrm{Ge_2}$ contributions, if refined together. To reduce this correlation, the same disorder parameter for both has been used. This approach eliminates the correlation and provides confidence in the assessment of relative structural changes between samples, although it may be less accurate in the assessment of absolute values of the disorder. A third $\mathrm{Sn-Ge_3}$ shell is found statistically significant around 4.8 Å but the relatively weak contribution does not allow to reliably quantify an eventual fraction of $\mathrm{Sn_3}$. In the third shell, therefore, only Ge neighbors are assumed. An example of best fit with partial contributions used in the analysis is presented in Fig. 4.

In samples M7-200 and M7-100, a nearest neighbor $\mathrm{Sn_1}$ shell is indispensable for the fit. This results in the R^2 factor [35] decreases by 20%; the F-Test [42] demonstrates a statistical significance, and thus can be considered reliable. The $R_{\mathrm{Sn_1}}$ distance is equal to the Sn-Sn distance in α-Sn (2.84 Å) and much less than the Sn-Sn bond length in β-Sn (3.05 Å), which suggests that in these samples a fraction of Sn atoms segregate in a pure α-Sn phase.

The $R_{\mathrm{Sn_2}}$ and $R_{\mathrm{Ge_2}}$ distances are very similar around 4.1 Å slightly expanded (+2.5%) with respect to the next neighbor distance in Ge crystal ($R_{\mathrm{Ge_2}} = 4.00$ Å), despite the quite different Sn-Ge and Ge-Ge bond lengths. This is not surprising, as it is well known that covalently bonded semiconductor alloys reduce the structural deformation induced by the rigid covalent bonds by modifying the bond angles [43]. It is important to highlight that there is a significant reduction in the deformation of interatomic distances with respect to pure Ge going from the first to the second coordination shell with a 5% and 2.5% change of R, respectively. Thus, the EXAFS results demonstrate local strain is much larger than the film strain being around 1% (Table I).

In all the samples except M7-200 and M7-100, the Sn appears bonded to 4 Ge at roughly the same distance $R =$ 2.58 Å. The relevance of Sn contribution in the second shell is evident in all the samples, ranging between 28% (sample C12-360) and 38% (M9-200, M11-200 samples), and reaching the largest fraction in M7-200 (45%) and M7-100 (40%) samples. This is much higher than would be expected from a random distribution of Sn atoms (e.g., 7.4% for M7-100), where the number of neighbors should be similar to the concentration of Sn in the sample. This finding, in agreement with previous reports [26,27], points out a nonrandom distribution of Sn around the average Sn site. While in the first shell, Sn-Sn bonds are energetically disadvantaged due to the quite long $R_{\mathrm{Sn_1}}$ covalent bond, there is a preference for the Sn second neighbor above the random distribution. This nonrandom Sn distribution implies some variation in Sn concentration at the atomic scale, with Sn richer units, having a higher fraction of Sn-Ge-Sn links, and Sn depleted regions, richer in Ge-Ge-Ge paths.

In general, we notice that while the interatomic distances are largely independent of Sn content or other deposition parameters, the structural disorder (MSRD,σ^2) depict an evident trend.

To examine the impact of the growth method on short-range order, $\mathrm{Ge_{1-x}Sn_x}$ films grown using MBE, at a low substrate temperature and growth rate, are compared with CVD grown samples that require a higher substrate temperature and growth rate. For direct comparison, the $\mathrm{Ge_{1-x}Sn_x}$ samples M11-200 and C11-330 have similar strain (−1.5%), Sn content (11 at. %), and thickness ($d_{\mathrm{M11-200/C11-330}} = 80/90$ nm) (Table II). The EXAFS analysis indicates very similar Sn local structure in both the samples either in the first coordination shell, with four Sn-Ge neighbors at 2.59 Å and similar disorder ($\sigma^2 \sim 2 \cdot 10^{-3}$ Å^2), and in the second coordination shell with $N_{\mathrm{Sn_2}}(N_{\mathrm{Ge_2}}) \sim$ 4.6(7.4) at $R_{\mathrm{Sn_2}}(R_{\mathrm{Ge_2}}) \sim 4.11(4.09)$ Å. The samples M11-200 and C11-330 have similar Sn content, thickness, and strain,

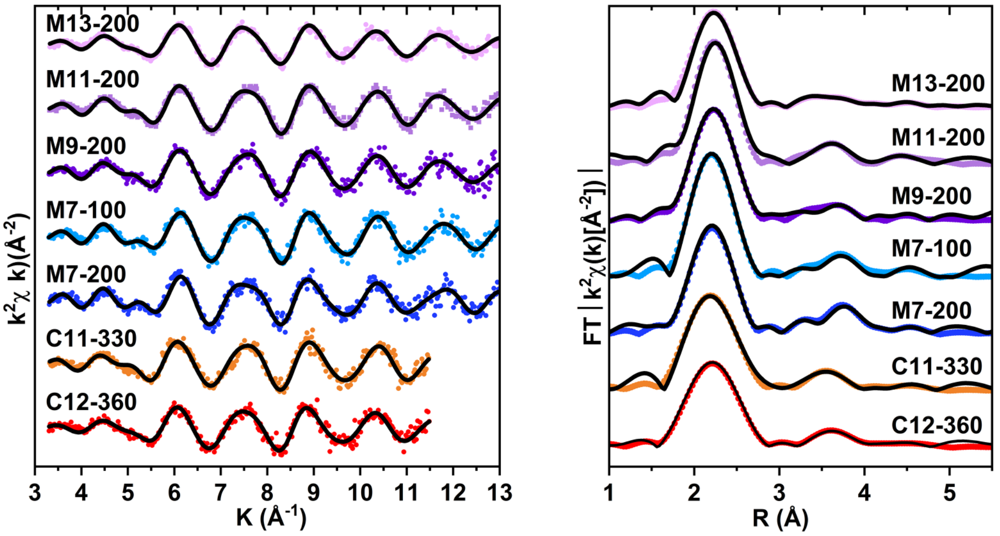

FIG. 3. The left panel presents the k^2 weighted experimental spectra (dots) and best-fit curves (full lines) of all the investigated samples, vertically shifted for clarity. Moduli of the Fourier transforms |FT| of k^2-weighted experimental data (dots) and best fit (full lines) are presented in the right panel, providing an intuitive image of the Sn neighbor distribution (see text).

although they were grown at $T_{M11-200} = 200\,^\circ C$ (MBE) and $T_{C11-330} = 330\,^\circ C$ (CVD), but no relevant Sn local structure changes (above the experimental uncertainties). This demonstrates that MBE and CVD techniques provide very similar Sn distribution in the films although growth conditions and methods are completely different.

Comparing the local structure of CVD samples C11-330 and C12-360, grown at comparable substrate temperatures (≈350 °C) and Sn content ($11 \leqslant x \leqslant 12\%$), offers information about the influence of lattice relaxation on the Sn short-range structure, as expected the thicker C12-360 sample has a smaller residual compressive strain (−0.6% strain),

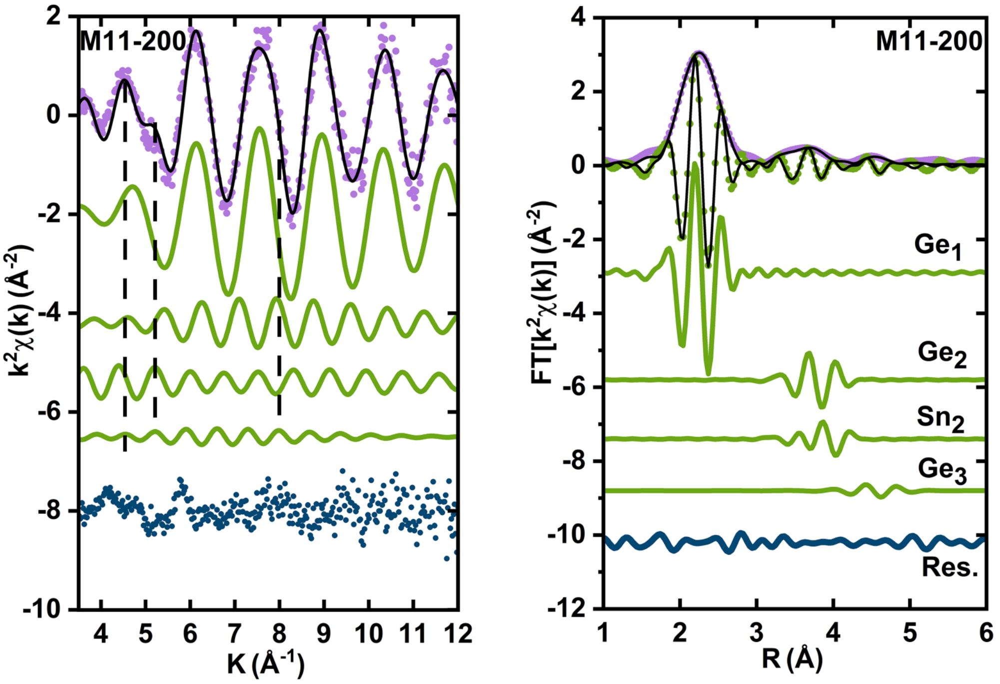

FIG. 4. Example of best fit of the EXAFS for sample M11-200. The k^2-weighted experimental data (dots), best-fit curve (full line), and partial contributions (vertically shifted for clarity) are shown in the left panel. The residual (experimental data–best fit) is also shown for comparison. The antiphase effect between the Sn−Ge$_2$ and Sn−Sn$_2$ is evident in the high k region of the data. In the low k regions of the spectrum ($4 - 6\,\text{Å}^{-1}$), the importance of the Sn−Sn$_2$ contribution in reproducing the tiny structural features is clear. The right panel shows the modulus and imaginary part of the FT of the k^2 weighted experimental data (dots) and best-fit curves (full lines). Imaginary parts of the FT of the partial contributions and residue are shown (vertically shifted for clarity).

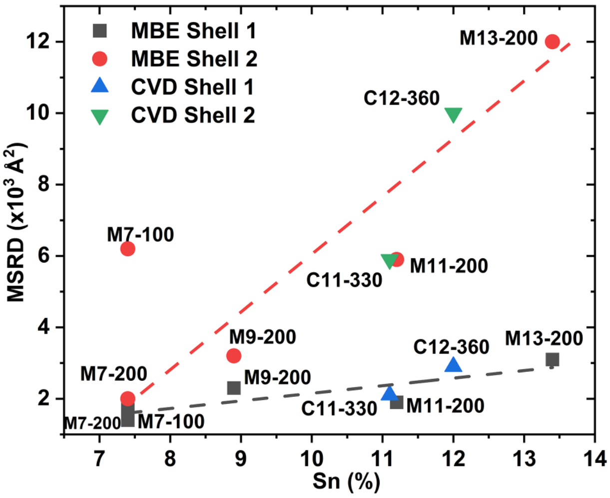

FIG. 5. The disorder factors (MSRD) from the EXAFS analysis in the first and second coordination shells for all MBE and CVD deposited samples as a function of Sn content. The larger noise for sample M7-100 (with low Sn content) is ascribable to the low deposition temperature. The dashed line serves as a guide to indicate the trend development for shell 1 and shell 2.

reflecting its increased relaxation. In the first shell, the Sn−Ge$_1$ distance is unchanged (within the error bar) for the two samples, reflecting the rigidity of the covalent Ge-Sn bond. On the contrary, the disorder is about 30% higher in the relaxed C12-360 samples. The effect of lattice relaxation is larger in the second Sn coordination shell that shows larger Sn$_2$ distance and reduced Sn$_2$ neighbors with respect to the strained layer. Also, in the second shell, the structural disorder increases for the relaxed sample pointing out a broader neighbor distribution, likely due to broader bond angle distribution.

The impact of growth temperature on the local structure of Ge$_{1-x}$Sn$_x$ films has been a hot topic of scientific debate in several publications. For instance, Liu *et al.* suggested that Ge$_{1-x}$Sn$_x$ films grown at lower temperatures exhibit more disorder, although they did not specify the temperature range [21]. Whereas, Lentz *et al.* reported more disorder at higher temperatures, comparing growth temperatures between 275 °C and 320 °C [28]. The M7-200 and M7-100 samples have the same Sn content (7.4 at.%), thickness (∼ 95 nm), and strain (−0.98%) but were grown at different substrate temperatures $T_{M7-200} = 200\,^{\circ}$C and $T_{M7-100} = 100\,^{\circ}$C, respectively. The EXAFS results (Table II) indicate the existence of Sn segregation in both samples and the overall Sn local coordination appears almost the same. However, note that M7-100 has a higher disorder in the second coordination shell, likely ascribed to the lower growth temperature.

The effect of Sn content on the local ordering is concluded in Fig. 5. Increasing the Sn content leads to more structural disorder of Sn in the first as well as in the second coordination shell in both MBE and CVD films. The effect is much larger in the second shell of the M7-100 sample and is ascribed to the low deposition temperature of 100 °C but the Sn segregation observed in this sample may also play a role. Certainly, lattice strain shows a similar trend because lattice strain and Sn content correlate to each other.

IV. CONCLUSION

We exploit the XAFS technique to explore the Sn-local atomic structure in a series of heteroepitaxial Ge$_{1-x}$Sn$_x$ thin films deposited by MBE and CVD, with different thicknesses and deposition temperatures.

The local Sn structure is similar in MBE and CVD grown samples, and the Sn-Ge/Sn interatomic distances in the first and second coordination shells are largely independent of the synthesis parameters. However, the deposition parameters have a significant effect on the local disorder around the Sn. In particular, increasing the Sn content and relaxation increases the disorder factors in the Sn coordination shells.

Importantly, the Sn-K edge EXAFS data analysis reveals a peculiar local chemical order favoring the heteroatomic Sn-Ge bonds, while the Sn-Ge-Sn configurations in the second coordination shell are systematically higher than expected from a random Sn distribution. This implies atomic scale inhomogeneities of Sn concentration along the film, despite the overall homogeneous Sn distribution. This peculiarity must be considered in order to gain a comprehensive understanding of the macroscopic properties of these films and to establish a correlation between the optoelectronic properties and the growth parameters.

Future studies, including a systematic investigation of GeSn films with varying thicknesses and relaxation states, will be necessary to fully understand this effect. Additionally, HAADF-STEM analysis can be beneficial to visualize Sn distribution directly in real space, further validating the local inhomogeneities concluded from EXAFS and offering a deeper understanding of strain relaxation and defect formation in GeSn films.

ACKNOWLEDGMENTS

We acknowledge the ESRF support for Proposal No. MA5463 and the valuable support of BM08-LISA beamline staff. Authors from Roma Tre acknowledge the financial support from MUR program "Dipartimenti di Eccellenza 2023–2027" (ART. 1, COMS. 314–337 LEGGE 232/2016), and Project ECS 0000024 Rome Technopole, NRP Mission 4 Component 2 Investment 1.5, Funded by the European Union–NextGenerationEU.

This work has also been carried out within the Joint Lab "Intelligent Electro-Optical Sensing," established between IHP and the University of Rome Tre.

DATA AVAILABILITY

The data that support the findings of this article are not publicly available. The data are available from the authors upon reasonable request.

[1] O. Moutanabbir *et al.*, Monolithic infrared silicon photonics: The rise of (Si)GeSn semiconductors, Appl. Phys. Lett. **118**, 110502 (2021).

[2] B. Marzban *et al.*, Strain engineered electrically pumped SiGeSn microring lasers on Si, ACS Photonics **10**, 217 (2023).

[3] Y. Junk *et al.*, Enhancing device performance with high electron mobility GeSn materials, Adv. Elect. Materials **11**, 2400561 (2024).

[4] A. Marchionni *et al.*, Inverse spin-Hall effect in GeSn, Appl. Phys. Lett. **118**, 212402 (2021).

[5] D. Spirito *et al.*, Thermoelectric efficiency of epitaxial GeSn alloys for integrated Si-based applications: Assessing the lattice thermal conductivity by raman thermometry, ACS Appl. Energy Mater. **4**, 7385 (2021).

[6] O. Concepción *et al.*, Isothermal heteroepitaxy of $Ge_{1-x}Sn_x$ structures for electronic and photonic applications, ACS Appl. Electron. Mater. **5**, 2268 (2023).

[7] P. Kaul *et al.*, Phase-coherent transport in GeSn alloys on Si, Adv. Elect. Materials **11**, 2400565 (2024).

[8] Y. Miao *et al.*, Review of Si-based GeSn CVD growth and optoelectronic applications, Nanomaterials **11**, 2556 (2021).

[9] D. Buca *et al.*, Room temperature lasing in GeSn microdisks enabled by strain engineering, Adv. Opt. Mater. **10**, 2201024 (2022).

[10] L. Seidel *et al.*, Continuous-wave electrically pumped multi-quantum-well laser based on group-IV semiconductors, Nat. Commun. **15**, 10502 (2024).

[11] V. Reboud *et al.*, Lasing in group-IV materials, in *Silicon Photonics IV*, edited by D. J. Lockwood and L. Pavesi, Topics in Applied Physics Vol. 139 (Springer, Cham, 2021), pp. 105–195.

[12] S. Gupta *et al.*, GeSn technology: Extending the Ge electronics roadmap, in *Proceedings IEEE International Electron Devices Meeting* (Washington, DC, 2011), pp. 16.6.1–16.6.4.

[13] D. Grützmacher, O. Concepción, Q.-T. Zhao, and D. Buca, Si–Ge–Sn alloys grown by chemical vapour deposition: A versatile material for photonics, electronics, and thermoelectrics, Appl. Phys. A **129**, 235 (2023).

[14] E. Kasper, M. Kittler, M. Oehme, and T. Arguirov, Germanium tin: Silicon photonics toward the mid-infrared [Invited], Photon. Res. **1**, 69 (2013).

[15] M. Oehme, K. Kostecki, M. Schmid, F. Oliveira, E. Kasper, and J. Schulze, Epitaxial growth of strained and unstrained GeSn alloys up to 25% Sn, Thin. Solid. Films **557**, 169 (2014).

[16] O. Gurdal *et al.*, Low-temperature growth and critical epitaxial thicknesses of fully strained metastable $Ge_{1-x}Sn_x$ ($x \lesssim 0.26$) alloys on Ge(001)2 × 1, J. Appl. Phys. **83**, 162 (1998).

[17] S. Wirths, D. Buca, and S. Mantl, Si–Ge–Sn alloys: From growth to applications, Prog. Cryst. Growth Charact. Mater. **62**, 1 (2016).

[18] A. A. Corley-Wiciak *et al.*, Local alloy order in a $Ge_{1-x}Sn_x/Ge$ epitaxial layer, Phys. Rev. Appl. **20**, 024021 (2023).

[19] T. Wendav *et al.*, Compositional dependence of the band-gap of $Ge_{1-x-y}Si_xSn_y$ alloys, Appl. Phys. Lett. **108**, 242104 (2016).

[20] S. Chen, X. Jin, W. Zhao, and T. Li, Intricate short-range order in GeSn alloys revealed by atomistic simulations with highly accurate and efficient machine-learning potentials, Phys. Rev. Mater. **8**, 043805 (2024).

[21] S. Liu *et al.*, 3D nanoscale mapping of short-range order in GeSn alloys, Small Methods **6**, 2200029 (2022).

[22] S. Liu *et al.*, Comparison of short-range order in gesn grown by molecular beam epitaxy and chemical vapor deposition, arXiv:2407.02767.

[23] S. Mukherjee *et al.*, Short-range atomic ordering in nonequilibrium silicon-germanium-tin semiconductors, Phys. Rev. B **95**, 161402 (2017).

[24] W. Dou *et al.*, Investigation of GeSn strain relaxation and spontaneous composition gradient for low-defect and high-Sn alloy growth, Sci. Rep. **8**, 5640 (2018).

[25] A. Elbaz *et al.*, Ultra-low threshold CW lasing in tensile strained GeSn microdisk cavities, in *Proceedings of the 2019 IEEE 16th International Conference on Group IV Photonics (GFP)* (IEEE, Singapore, Singapore, 2019), pp. 1–2.

[26] B. Cao, S. Chen, X. Jin, J. Liu, and T. Li, Short-Range Order in GeSn Alloy, ACS Appl. Mater. Interfaces **12**, 57245 (2020).

[27] F. Gencarelli *et al.*, Extended X-ray absorption fine structure investigation of Sn local environment in strained and relaxed epitaxial $Ge_{1-x}Sn_x$ films, J. Appl. Phys. **117**, 095702 (2015).

[28] J. Z. Lentz *et al.*, Local ordering in Ge/Ge–Sn semiconductor alloy core/shell nanowires revealed by extended x-ray absorption fine structure (EXAFS), Appl. Phys. Lett. **122**, 062103 (2023).

[29] G. Bera *et al.*, Local structural investigation across the magnetic transition in the type-II multiferroic material $FeVO_4$, Phys. Rev. B **109**, 075138 (2024).

[30] E. Kamiyama *et al.*, Analysis for positions of Sn atoms in epitaxial $Ge_{1-x}Sn_x$ film in low temperature depositions, Thin. Solid. Films **557**, 173 (2014).

[31] Y. L. Soo *et al.*, Substitutional incorporation of Sn in compressively strained thin films of heavily-alloyed $Ge_{1-x}Sn_x/Ge$ semiconductor probed by x-ray absorption and diffraction methods, Semicond. Sci. Technol. **29**, 115008 (2014).

[32] Gencarelli *et al.*, Crystalline Properties and Strain Relaxation Mechanism of CVD Grown GeSn, ECS J. Solid State Sci. Technol. **2**, P134 (2013).

[33] F. d'Acapito *et al.*, The LISA beamline at ESRF, J. Synchrotron Rad. **26**, 551 (2019).

[34] C. Meneghini *et al.*, Antiferromagnetic–paramagnetic insulating transition in Cr-doped V_2O_3 investigated by EXAFS analysis, J. Phys.: Condens. Matter **21**, 355401 (2009).

[35] C. Meneghini, F. Bardelli, and S. Mobilio, ESTRA-FitEXA: A software package for EXAFS data analysis, Nucl. Instrum. Methods Phys. Res. Sect. B **285**, 153 (2012).

[36] F. James, "Function minimization and error analysis reference manual." CERN Program Library Long Writeup D506 (1994), https://cds.cern.ch/record/2296388?ln=en.

[37] J. J. Rehr and R. C. Albers, Theoretical approaches to x-ray absorption fine structure, Rev. Mod. Phys. **72**, 621 (2000).

[38] A. L. Ankudinov, C. E. Bouldin, J. J. Rehr, J. Sims, and H. Hung, Parallel calculation of electron multiple scattering using Lanczos algorithms, Phys. Rev. B **65**, 104107 (2002).

[39] Y. Nishino, S. Muramatsu, Y. Takano, and H. Kajiyama, Extended x-ray-absorption fine-structure study of hydrogenated amorphous silicon-germanium alloys. II. Dependence of bond length and coordination on composition, Phys. Rev. B **38**, 1942 (1988).

[40] R. Pöttgen, Stannides and intermetallic tin compounds–fundamentals and applications, Zeitschrift Für Naturforschung B **61**, 677 (2006).

[41] J. B. Boyce and J. C. Mikkelsen, Local structure of pseudobinary semiconductor alloys: An x-ray absorption fine structure study, J. Cryst. Growth **98**, 37 (1989).

[42] A. Michalowicz, K. Provost, S. Laruelle, A. Mimouni, and G. Vlaic, F-test in EXAFS fitting of structural models, J. Synchrotron Rad. **6**, 233 (1999).

[43] F. Boscherini, C. Lamberti, S. Pascarelli, C. Rigo, and S. Mobilio, Local atomic structure in strained interfaces of $\mathrm{In}_x\mathrm{Ga}_{1-x}\mathrm{As}/\mathrm{InP}$ heterostructures, Phys. Rev. B **58**, 10745 (1998).